Proceedings of the ASME 2024
International Mechanical Engineering Congress and Exposition
IMECE2024
November 17-21, 2024, Portland, Oregon, USA

IMECE2024-139667

A COMPUTATIONAL FLUID DYNAMICS MODEL FOR INVESTIGATION OF MATERIAL TRANSPORT THROUGH THE VIRTUAL IMPACTOR IN AEROSOL JET PRINTING

Akashita Sareen
Department of Mechanical & Industrial Engineering, Marshall University, Huntington, WV 25755, USA

Curtis W. Hill
NASA Marshall Space Flight Center, ESSCA, Huntsville, AL 35808, USA

Roozbeh "Ross" Salary *
Departments of Mechanical & Biomedical Engineering, Marshall University, Huntington, WV 25755, USA

ABSTRACT

Aerosol jet printing (AJP) is a direct-write additive manufacturing technique used to fabricate electronics, such as sensors, capacitors, and optoelectronic devices. It has gained significant attention in being able to utilize aerodynamic principles to deposit conductive inks (such as silver nanoparticle-based inks) onto rigid and flexible substrates. The aerosol jet printing system consists of three main components to execute the printing process: (i) the pneumatic atomizer, (ii) the virtual impactor, and (iii) the deposition head. The virtual impactor (VI) lies between the pneumatic atomizer and the deposition head, accepting the accelerated flow of differently sized aerosol particles from the pneumatic atomizer, while acting as an "aerodynamic separator." With the challenges associated with the efficiency as well as resulting quality of the AJP process, the virtual impactor presents a unique opportunity to gain a deeper understanding of the component itself, aerosol particle flow behavior, and how it contributes to overall printing inefficiencies, poor repeatability, and resulting print quality. Broadly, this effort enables the expedited adoption of AJP in the electronics industry and beyond at large scales. The challenges mentioned are addressed in this work by conducting a computational fluid dynamics (CFD) study of the virtual impactor to visualize fluid transportation and deposition under specific conditions.

The objective of this study is to observe and characterize a single-phase, compressible, turbulent flow through the virtual impactor in AJP. The virtual impactor geometry is modeled in the ANSYS-Fluent environment based on the design by Optomec. The virtual impactor is assembled using a housing, collector, jet, stem, O-rings and a retaining nut. Subsequently, a mesh structure is generated to discretize the flow domain. In addition, material properties, boundary conditions, and the relevant governing equations (based on the Navier-Stokes equations) are utilized to, ultimately, generate an accurate steady-state solution. The fluid flow is examined with respect to mass flow rates set at boundary conditions. The aerosol particles' interactions with the inner walls of the virtual impactor are observed. Particularly, an insight into the characteristics of aerosol particles entering the virtual impactor and their transition into a smoother flow before entering the deposition head is gained. Furthermore, the analysis provides an opportunity to observe fluid flow separation based on the design of the virtual impactor, one of its main functions in the AJP process. This exposes probable causes for inaccurate print quality, flow blockages, inconsistent outputs, process instability, and other material transport inefficiencies. Overall, this research work lays the foundation for improvements in the knowledge and performance of aerosol jet printing's virtual impactor toward optimal fabrication of printed electronics.

KEYWORDS

Advanced Manufacturing; Aerosol Jet Printing (AJP); Computational Fluid Dynamics (CFD); Printed Electronics

NOMENCLATURE

AGFR	Atomization Gas Flow Rate
AJP	Aerosol Jet Printing
CFD	Computational Fluid Dynamics
EGFR	Exhaust Gas Flow Rate
PA	Pneumatic Atomizer
SCCM	Standard Cubic Centimeter per Minute
VI	Virtual Impactor

* Contact author. Tel.: +1(315)395-4598; fax: +1(304)696-5454; e-mail address: salary@marshall.edu.

1. INTRODUCTION

1.1. Goals and Objectives

Among manufacturing techniques that have been used for fabrication of printed electronics, such as continuous/drop-on-demand inkjet printing, stencil printing, screen printing, gravure printing, and extrusion printing [1-3], the pneumatic-based aerosol jet printing (AJP) process has the potential for fast and accurate production of electronic devices. It has emerged as one of the processes that meets the intricate printing requirements of various electronic devices based on designs, substrates, inks, etc. [4]. In addition, the underlying aerodynamics of the system contribute to making the printing process more streamlined and focused resulting in a more precise print quality. The VI in the pneumatic-based AJP ensures this streamlined flow of aerosols by removing excess gas from the system before transporting the material into the deposition head [5]. Combining this knowledge with CFD modeling presents the inner workings of the VI which lead to viable improvements in the overall efficiency and effectiveness of the entire AJP system.

This paper's objective is to establish a 3D-CFD model of the VI simulated under single-phase, compressible, and turbulent flow conditions. The pneumatic-based AJP process undergoes high pressure, pneumatic atomization of a functional ink using a flow of air or nitrogen gas. The gas flow acts as a carrier for the non-uniform aerosol particles moving with high velocity from the atomizer through the VI to the deposition head as a multi-phase flow [4]. In addition, it has been observed that the pneumatic generation and deposition of aerosols on a free surface are based on high velocity, turbulent flows [6, 7]. Furthermore, the high velocity aerosol transport and deposition in AJP require compressible and turbulent flow modeling [1]. Therefore, the flow of aerosols in AJP is inherently a multi-phase, compressible, and turbulent flow, which should be incorporated in CFD modeling of AJP.

The single-phase, turbulent, and compressible CFD modeling presented in this study is the primary step toward understanding and visualizing flow behavior in the VI. Observing the gas flow through the VI geometry validates the 3D model and sheds light on its effectiveness to expel gas flow at the EGF port as well as through the collector tube. The 3D CFD model of the VI plays an important role in understanding fluid behavior. It sets the foundation to study the pneumatic atomizer and nozzle head in integration with the VI for better AJP results.

1.2. Literature Review

According to Wilkinson *et al.*, the AJP process captures a wide range of applications in various industries [8]. It is widely known for its flexibility in being used with different materials and geometries. Hines *et al.* state that the AJP technology can be used to replace traditional techniques as long as the technology can be improved to a degree that complex structures of electronics can be produced [9]. Several experimental and numerical assessments have been made of the printing system on flexible electronic devices [10]. In addition, the AJP has also been evaluated from a control standpoint [11]. Recently, Rurup *et al.* have conducted experiments based on software control of the AJP for improving print reliability indicating that real time monitoring of the system yields beneficial results [12]. According to Guyll *et al.*, temperature plays a crucial role in determining stability, throughput, and resolution of the AJP process. By heating the print head, the system underwent an increase in process reliability [13]. In a newer application in the area of soft robotics, Karipoth *et al.* found that the AJP process can be used to develop flexible strain sensors to attach to robotic devices [14]. Smith *et al.*, prove that the AJP process is an advantageous path to decrease cost and complexity while printing structures that require structural supports and long post processing which in turn improve mechanical reliability and aesthetic appearance [15]. Such unique capabilities are supported by deconstructing the AJP process itself, especially in the way that Meredith *et al.* conduct their study by developing an *in-situ* droplet imaging system that displays the droplets and their sizes between the printer nozzle and the relevant substrate. They perform this study non-invasively leading to the in-flight monitoring of the system for closed loop control and feedback [16]. All these studies indicate the potential that further research using different techniques could unravel and that there are different ways to consider AJP efficiencies in terms of control, temperature, and droplet size monitoring.

Several research works have also identified and addressed the application of CFD in the analysis and improvement of the AJP. For instance, Chen *et al.* developed a CFD model to visualize the flow of the carrier gas through the system [17]. They conclude that their analysis provides an insight into operating parameters of the system as enabled by the CFD process. Another study by Ramesh *et al.*, investigates aerosol jet printing through a CFD lens and draws attention to the advantages of the AJP process that directly impact the optimization of the printer and prediction of defect occurrence [18]. Lastly, a CFD analysis is conducted by Salary *et al.* focusing on the pneumatic atomizer and deposition head to gain insights into the internal environment of the AJP process [7].

While these works have concluded results in predominantly the pneumatic atomizer and nozzle or deposition head of the AJP, the virtual impactor has not been sufficiently modeled or investigated for its impact on the printing system. The VI component is deemed a powerful part of the AJP with its ability to transform chaotic turbulent flow into a concentrated and uniform flow of aerosols. If done so, AJP can be implemented faster in all the wide areas of applications discussed before. Between the two types of AJP processes, the pneumatic-based process with the VI works better for high viscosity fluids such as paste inks [19], while the ultrasonic-based process works better for low viscosity inks and produces aerosols of more uniform size [20]. Therefore, there is no need to use VI together with ultrasonic atomization. The VI is exclusively a part of the pneumatic based AJP process overcoming the hurdles of scattered and non-uniform aerosol particles that are delivered to the printing head prior to deposition on a free surface. The turbulent atomization flow results in high pressure, accelerated formation of non-uniform ink particles carried from the

pneumatic atomizer toward the VI via the aid of the gas flow. Ordinarily, a typical VI system in the AJP process would separate large and small droplets of aerosol, creating a uniform major flow of highly dense particles for printing; this is inevitable to achieve optimal printing outcomes with no scatter and high precision [1]. Please note that the CFD model presented in this work will aid in studying aerosol generation and transport in the AJP process, particularly when pneumatic atomization is the method of choice for aerosol generation. The outcomes of this work can be integrated with future modeling of the deposition head as well as the pneumatic atomizer toward optimal fabrication of electronic devices.

Given all the applications of the AJP and the advantages of using CFD for modeling will help in applying the same idea to the VI. Kim *et al.*, suggest design modifications to the VI and their analysis has resulted in better performance of the component for each design iteration [21].

The above-mentioned review of literature shows that there has been adequate consideration and analysis given to the main components of AJP, such as the pneumatic atomizer and the deposition head. Experimental studies have set the foundation for analyzing and examining the VI and its contributions to print quality in AJP. However, there is a gap in knowledge and understanding in terms of aerodynamic aerosol transport and separation in the VI, which requires investigation of the function of VI and its influence on print quality, repeatability, and efficiency in the AJP process. This gap is addressed in this work by establishing an advanced CFD model to understand the aerodynamics of aerosol flow in AJP process. The CFD model in terms of geometry, meshing, and boundary conditions are discussed in Sec. 2. In addition, the results of the CFD models are discussed in Sec. 3. Finally, the main observations and conclusions of the work are presented in Sec. 4.

2. MATERIAL AND METHODS

2.1. Materials

Steel is assigned as the material to the VI including its housing, impactor, collector, stem, and exhaust gas flow outlet as all these parts are treated as one solid, as shown in Figure 1(a). The fluid that passes through the cavity of the VI is set to nitrogen gas replicating the flow through the AJP, as schematically demonstrated in Figure 1(b), where aerosols are carried through the system via nitrogen [7].

2.2. Computational Fluid Dynamics (CFD)

2.2.1. Virtual Impactor (VI) Design

The geometry of the VI is developed in the ANSYS Fluent environment based on Optomec's design captured in an x-ray image as well as images of its components obtained from a previous research work [7] in the literature. As seen in Figure 1, the design consists of the main VI components, namely, housing, stem, impactor, collector, and the exhaust gas flow (EGF).

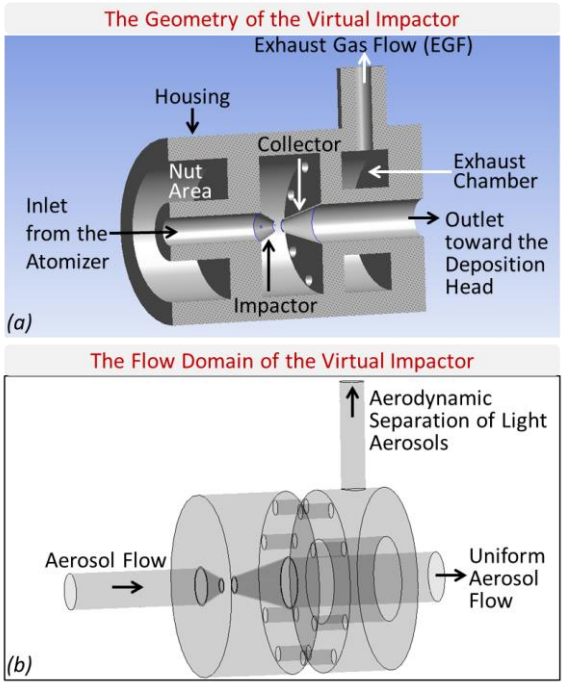

Figure 1: THE GEOMETRY AND FLOW DOMAIN OF THE VIRTUAL IMPACTOR IN AJP.

A thorough dimensional analysis, according to Table 1, was conducted based on the available images and references yielding an efficient and proportional model for analysis. The resulting geometries included solid and fluid domains for the CFD analysis.

Table 1: DIMENSIONS OF THE VI USED IN THE 3D MODEL.

Dimension Name	Value [in]
Housing Length	1.5680
Housing Diameter	0.9964
Stem Length	0.3691
Stem Inner Diameter	0.1503
Stem Outer Diameter	0.3136
Impactor Plate Thickness	0.1993
Impactor Nozzle Length	0.0882
Impactor Top Diameter	0.0506
Impactor Base Diameter	0.1503
Distance Between Impactor and Collector Plate	0.3822
Distance Between Impactor and Collector	0.0555
Collector Nozzle Length	0.2385
Collector Nozzle Base Diameter	0.2058
Collector Nozzle Top Diameter	0.0621
Collector Plate Thickness	0.1241
Collector Length	0.2940
Collector Tube Inner Diameter	0.2058
Collector Tube Outer Diameter	0.3495
EGF Inner Diameter	0.1013
EGF Outer Diameter	0.2842
EGF Height	0.3005
Housing Exit Wall Thickness	0.2123
Collector Pores Diameter	0.0621
Collector Pore Position (Top Set, Horizontal)	0.1533

Dimension Name	Value [in]
Collector Pore Position (Top Set, Vertical)	0.3000
Collector Pore Position (Bottom Set, Vertical)	0.1500
Collector Pore Position (Bottom Set, Horizontal)	0.3028

2.2.2. Meshing

The fluid domain, i.e., the inner cavity of the VI is meshed using 4-node tetrahedron elements having an element size of 0.10624 [in]. The mesh generated 28,099 nodes and 137,252 elements.

2.2.3. Governing Equations in CFD Analysis

The Navier Stokes equation forms the basis of this study for the resulting CFD simulation for a steady-state solution where density and viscosity are kept constant.

$$\rho \frac{\partial u}{\partial t} - \mu \nabla^2 u + \rho(u.\nabla)u + \nabla p = F \qquad (1)$$

In the above equation, ρ, u, and μ are density [kg/m^3], velocity [m/s], and dynamic viscosity [kg/m.s], respectively. ∇ is the mathematical del operator, p is pressure [Pa], and F is forces [N] in the system [7].

2.2.4. Fluid Properties and Boundary Conditions

The fluid properties play a significant role in the CFD analysis. Initially, air was used to test if the model performed a basic simulation of fluid passing through cavities with set parameters. Once this was tested for the simulation, the movement of nitrogen gas through the geometry of the VI is analyzed. The properties of Nitrogen are set as 1.138 [kg/m^3] for density and 1.663 E-05 [kg/m.s] for viscosity.

The viscous standard k-epsilon model with standard wall functions for near wall treatment is used. The boundary conditions for the simulation are set at the inlet, outlet, EGF, and wall as seen in Figure 1. The gas flow rate values have been obtained as shown in Table 2. The atomization gas flow rate (AGFR) is set as the mass flow at the inlet of the VI under the absolute frame of reference with an initial gauge pressure of 0 [Pa]. The turbulence specification method is set to intensity and viscosity ratio with turbulence intensity of 1% and turbulence viscosity ratio of 10. The exhaust gas flow rate (EGFR) is set as the mass flow at the EGF. The difference between the AGFR and EGFR is set as the mass flow rate at the outlet of the VI [7]. Lastly, a stationary wall with no-slip condition and a standard roughness model is used.

Table 2: BOUNDARY CONDITIONS AT THE VI INLET (AGFR), EGF (EGFR), AND VI OUTLET.

Boundary Name	Boundary Type	Boundary Value
AGF Inlet	Mass Flow Rate	500 [SCCM] 8.30 E-06 [m3/s] 9.48 E-06 [kg/s]
EGF Outlet	Mass Flow Rate	450 [SCCM] 7.50 E-06 [m3/s] 8.53 E-06 [kg/s]
VI Outlet	Mass Flow Rate	50 [SCCM] 0.83 E-06 [m3/s] 0.95 E-06 [kg/s]
VI Wall	No-Slip	N/A

2.2.5. Numerical Solutions

The numerical setup for the CFD simulation includes a coupled scheme. In the spatial discretization setup, the gradient is selected as the least squares cell based along with second order pressure, second order upwind momentum, second order upwind turbulent kinetic energy, and lastly, second order upwind turbulent dissipation rate. The pseudo time method is chosen as the global time step for the purposes of this analysis.

Solution initialization includes standard initialization with a relative to cell zone reference frame. Initial values of 0.740417 [m/s] x-direction velocity, 8.223261E-05 [m^2/s^2] turbulent kinetic energy, and 4.16467E-06 [m^2/s^3] turbulent dissipation rate are used.

2.2.6. Verification

Verification of the analysis is done by probing the boundary conditions (as reported in Table 2) on the pressure and velocity results. The specified boundary conditions such as the inlet, outlet, and EGF remained closely at the set boundary values for all simulations.

3. RESULTS AND DISCUSSION

3.1. Velocity Contour Analysis

The simulation results are shown in the velocity contour plot in Figure 2. The nitrogen gas moves through the first tube of the system called the stem at a uniform velocity. As the flow passes through the impactor's outlet, which is the first nozzle, it accelerates at a high velocity. The impactor and collector geometry and placement resembles a converging-diverging model.

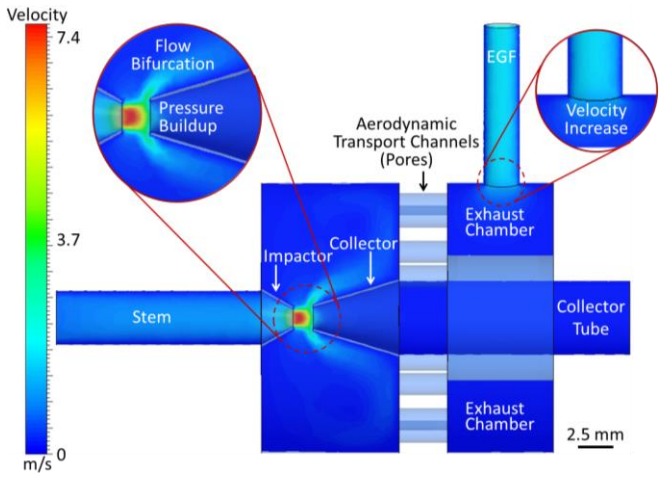

Figure 2: VELOCITY CONTOUR ANALYSIS OF THE VIRTUAL IMPACTOR.

This phenomenon is visible in the contour plot as the color changes from blue to yellow in the middle of the impactor and

collector but is placed closer to the impactor. In AJP multi-phase simulation, aerosol particles are injected of different sizes along with nitrogen gas flow, this acceleration and an active mass flow rate condition at the EGF aids in the separation of such particles as the smaller and lighter particles are exhausted out of the system through the EGF, while the larger and heavier particles pass through the collector and into the deposition head resulting in a uniform flow with uniformly sized particles. As evident from Figure 2, the flow bifurcation illustrates the VI's main function in the AJP process as an "aerodynamic separator". Effective bifurcation results in stable and collimated ink deposition during printing.

This bifurcation is marked by the acceleration observed in the bright yellow and scattered flow in the contour in Figure 2. The high velocity indicated at the position between the impactor and collector also marks a pressure buildup leading to the bifurcation seen in the contour. It is important to note that the top diameter of the impactor is smaller than the top diameter of the collector at 0.0506 [in] and 0.0621 [in], respectively. The bifurcation is also prominent due to the cone-like shape of the collector.

Following this interaction, the fluid is seen to travel a relatively longer distance than the length of the impactor to reach the collector plate's aerodynamic transport channels (referred to as pores). The pores are designed according to images obtained of the components which serve the purpose of diverting the lighter and smaller particles into the exhaust chamber for their exit through the EGF. The pores' diameter is set equal to the diameter of the collector's top diameter as observed in component images from the literature.

There are eight such pores that transport the fluid into the exhaust chamber. Once into the exhaust chamber, the velocity of the fluid is seen to increase as it exits the EGF. This is visible in the contour in the cylinder of the EGF. As a result, it can be verified that the boundary conditions enable the current flow of fluid through the system.

It must be noted that experiments with different boundary conditions will yield results comparable to the functioning of the VI in the AJP. For example, individual velocity and pressure boundary conditions will present interesting insights to observe. The introduction of a multi-phase flow in CFD would also present new contour relationships to decipher the fluid performance closest to an actual AJP process. An additional mass flow rate boundary condition could also be set at the inlet of the collector to gain more control over the process of fluid separation and transportation through the collector's tube.

3.2. Velocity Streamline Analysis

In Figure 3 below, a streamline analysis is conducted of the fluid. It can be observed that the fluid takes the shape of the cylindrical stem and the conical shape of the impactor. As it reaches the acceleration point (near the impactor's exit), the streamline can be observed to be entering through the collector's nozzle, thereby taking its shape, as well as slowing down while moving through the collector's tube.

In addition, the streamline is also observed to move in a circular motion in the lower portion of the first chamber where the impactor and collector are present. The circular fluid motion indicates accumulation of the fluid in the lower chamber. However, the upper portion of the chamber experiences no such behavior and fluid flows through the pores into the exhaust chamber without circulation and stagnation in the first chamber. This could be due to the geometry of the collector's conical nozzle at the lower end with which the fluid interacts and remains in the chamber. Additionally, the placement of the EGF port could also contribute to the circulation and buildup of the particles in the lower chamber with non-uniform removal of lighter aerosol particles. Particle buildup in the lower chamber suggests saturation and accumulation of ink in the first and exhaust chambers. This implies that the lighter and smaller particles would be transported through the collector tube along with the larger and heavier particles resulting in overspray as the flow exits the deposition head. Such behavior causes a negative impact on printing quality. Moreover, it becomes challenging to periodically dismantle and clean the component causing delays in the printing process and a gradual decline in printing repeatability of AJP.

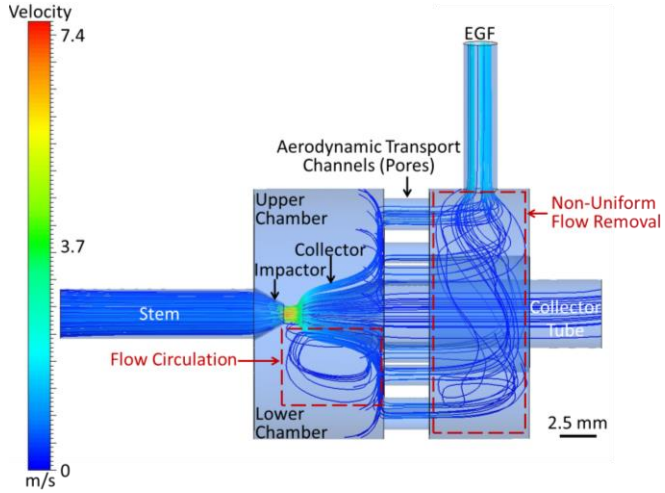

Figure 3: VELOCITY STREAMLINE ANALYSIS OF THE VIRTUAL IMPACTOR.

The streamline plot also shows the movement of the fluid through the aerodynamic transport channels (pores). All eight pores experience the fluid passing through them and reaching the exhaust chamber. The swirling of the fluid is visible with the streamline in the exhaust chamber as it moves around the collector's tube and reaches the EGF. The EGF shows that the fluid exits from it at a greater velocity corresponding to the set mass flow rate.

In Figure 4, the velocity of the fluid moving through the pores of the collector plate is higher than the velocity of the fluid through the collector tube. This verifies the analogy that a stable and uniform flow can be expected out of the current design of the VI. Furthermore, this observation validates the 3D model developed, and the boundary conditions set for the study as fluid

exits the VI as expected. Figure 4 also shows the interaction of the fluid particles in the exhaust chamber as they meet the exit wall and get diverted to the EGF. The fluid particles in the lower portion of the exhaust chamber must move around the collector tube to reach EGF.

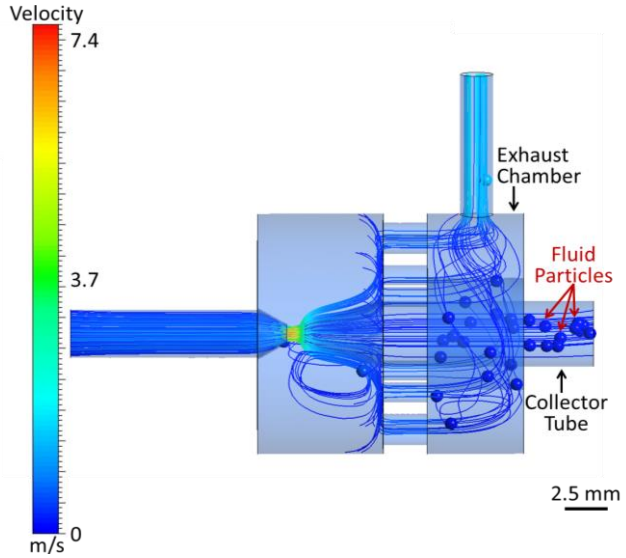

Figure 4: VELOCITY STREAMLINE ANALYSIS OF THE VIRTUAL IMPACTOR WITH PARTICLES GOING THROUGH THE COLLECTOR TUBE AND THE EXHAUST CHAMBER.

Varying diameters of the impactor, collector, and collector pores could present modified fluid behavior which could be utilized in different applications of the AJP. The fluid exiting from the collector tube could be more or less dense as a result of the change in diameters. For example, the current experiment could work better for one industry over the other. The impactor and collector could also be joined with a porous surface to prevent the loss of fluid and the buildup of fluid or ink in the first chamber. The EGF may be placed in different locations or additional EGF could be added to simulate uniform removal of fluid from both the chambers. These changes could ensure consistency in printing results.

3.3. Pressure Contour Analysis

According to Figure 5, the impactor's stem experiences the highest pressure in the model as the fluid is injected through it at a high velocity. This can be seen with the striking red color in the stem of the impactor. The whole area experiences the same amount of pressure as the fluid exits out of the impactor.

The first chamber as well as the exhaust chamber experience a relatively lower pressure in them as the fluid moves through. Once the flow acceleration takes place, the collector and its tube experience significant pressure as well, as can be seen in yellow. This is also indicative of the fluid moving through at a slower and more uniform rate as it passes through the collector. Upon exit through the EGF, the pressure begins to decrease and stabilize. As discussed earlier, this observation is in conjunction with comparatively uniform and stable velocity of the flow through the collector tube.

Future CFD experiments of the AJP are supported by this change in pressure observed as the fluid moves from the impactor to the collector. It indicates that modifications in the flow rate at the inlet and outlet would affect the pressure that the parts experience. Particularly, higher flow rate would correspond to higher pressure on the part through which the fluid is moving and vice versa. Optimum inlet and outlet flow rates would ensure that the pressure of the fluid does not disrupt the flow of the fluid by over-deposition or clogging in the VI. This would lead to uniform and concise printing outcomes.

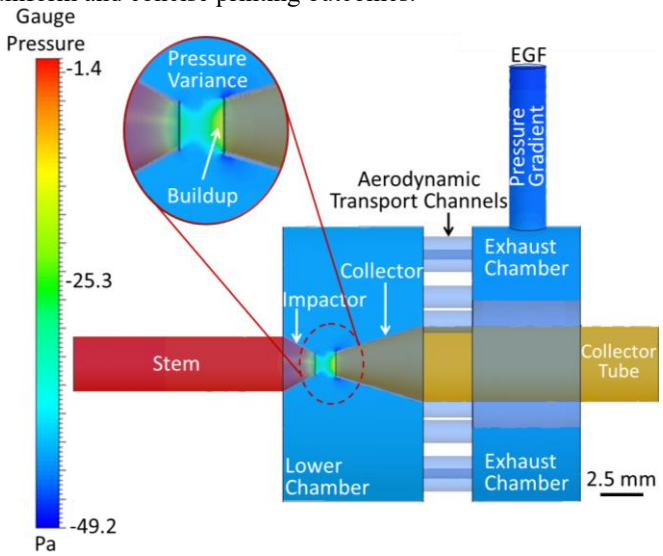

Figure 5: PRESSURE CONTOUR ANALYSIS OF THE VIRTUAL IMPACTOR.

4. CONCLUSIONS AND FUTURE WORK

4.1. Conclusions

The following main conclusions can be drawn based on the results of this study.

- Accelerated flow was observed at the exit and entrance of the impactor and collector, respectively.
- Flow bifurcation was observed in the space between the impactor and collector.
- It was observed that the velocity of the fluid increases as it exits the EGF (after the exhaust chamber).
- Circulation was observed in the lower portion of the first chamber, while no such circulation was observed in the upper portion. This could be due to the presence of the EGF port, which is closer to the upper portion, leading to relatively stronger removal of fluid particles, preventing formation of a circular flow pattern in the upper chamber.
- The fluid exits EGF at a higher velocity than the VI outlet.
- More uniform flow was observed at the collector as well as through the collector tube.
- The flow within the exhaust chamber began to swirl prior to exiting toward the EGF.
- Maximum pressure was observed within the stem as well as the impactor, followed by the pressure in the collector tube.

4.2. Future Work

The current effort has set the foundation to further explore the aerodynamic properties of fluid flowing through the VI. Future work entails running additional simulations on modified geometries of the VI. Fluid properties used in the analysis can be enhanced and a multi-phase flow can be introduced.

ACKNOWLEDGMENTS

Dr. Salary would like to thank the National Science Foundation (NSF) for funding this work under award # *OIA-2327460*.

REFERENCES

[1] Secor, E. B., 2018, "Principles of Aerosol Jet Printing," Flexible and Printed Electronics, 3(3), p. 035002, DOI: 10.1088/2058-8585/aace28.

[2] Deiner, L. J., and Reitz, T. L., 2017, "Inkjet and Aerosol Jet Printing of Electrochemical Devices for Energy Conversion and Storage," Advanced Engineering Materials, 19(7), p. 1600878, DOI: 10.1002/adem.201600878.

[3] Gamba, L., Johnson, Z. T., Atterberg, J., Diaz-Arauzo, S., Downing, J. R., Claussen, J. C., Hersam, M. C., and Secor, E. B., 2023, "Systematic Design of a Graphene Ink Formulation for Aerosol Jet Printing," ACS Applied Materials & Interfaces, 15(2), pp. 3325-3335, DOI: 10.1021/acsami.2c18838.

[4] Balani, S. B., Ghaffar, S. H., Chougan, M., Pei, E., and Şahin, E., 2021, "Processes and Materials Used for Direct Writing Technologies: A Review," Results in Engineering, 11, p. 100257, DOI: 10.1016/j.rineng.2021.100257.

[5] Jeong, H., Lee, J. H., Kim, S., Han, S., Moon, H., Song, J.-Y., and Park, A.-Y., 2023, "Optimization of Process Parameters in Micro-Scale Pneumatic Aerosol Jet Printing for High-Yield Precise Electrodes," Scientific Reports, 13(1), p. 21297, DOI: 10.1038/s41598-023-47544-4.

[6] Salary, R., Lombardi, J. P., Tootooni, M. S., Donovan, R., Rao, P. K., Borgesen, P., and Poliks, M. D., 2017, "Computational Fluid Dynamics Modeling and Online Monitoring of Aerosol Jet Printing Process," Journal of Manufacturing Science and Engineering, 139(2), p. 021015, DOI: 10.1115/1.4034591.

[7] Salary, R., Lombardi, J. P., Weerawarne, D. L., Rao, P., and Poliks, M. D., 2021, "A Computational Fluid Dynamics Investigation of Pneumatic Atomization, Aerosol Transport, and Deposition in Aerosol Jet Printing Process," Journal of Micro- and Nano-Manufacturing, 9(1), p. 010903, DOI: 10.1115/1.4049958.

[8] Wilkinson, N., Smith, M., Kay, R., and Harris, R., 2019, "A Review of Aerosol Jet Printing — A Non-traditional Hybrid Process for Micro-manufacturing," The International Journal of Advanced Manufacturing Technology, 105, pp. 4599-4619, DOI: 10.1007/s00170-019-03438-2.

[9] Hines, D., Gu, Y., Martin, A., Li, P., Fleischer, J., Clough-Paez, A., Stackhouse, G., Dasgupta, A., and Das, S., 2021, "Considerations of Aerosol-Jet Printing for the Fabrication of Printed Hybrid Electronic Circuits," Additive Manufacturing, 47, p. 102325, DOI: 10.1016/j.addma.2021.102325.

[10] Zhang, Y., Zhu, T., Jiao, J., Song, S., Wang, Z., and Wang, Z., 2023, "Experimental and Numerical Investigation on the Aerosol Micro-Jet 3D Printing of Flexible Electronic Devices," Materials, 16(22), p. 7099, DOI: 10.3390/ma16227099.

[11] Smith, M., Choi, Y. S., Boughey, C., and Kar-Narayan, S., 2017, "Controlling and Assessing the Quality of Aerosol Jet Printed Features for Large Area and Flexible Electronics," Flexible and Printed Electronics, 2(1), p. 015004, DOI: 10.1088/2058-8585/aa5af9.

[12] Rurup, J. D., and Secor, E. B., 2024, "A Real-Time Process Diagnostic to Support Reliability, Control, and Fundamental Understanding in Aerosol Jet Printing," Advanced Engineering Materials, 26(1), p. 2301348, DOI: doi.org/10.1002/adem.202301348.

[13] Guyll, B. I., Petersen, L. D., Pint, C. L., and Secor, E. B., 2024, "Enhanced Resolution, Throughput, and Stability of Aerosol Jet Printing via In Line Heating," Advanced Functional Materials, p. 2316426, DOI: 10.1002/adfm.202316426.

[14] Karipoth, P., Chandler, J. H., Lee, J., Taccola, S., Macdonald, J., Valdastri, P., and Harris, R. A., 2024, "Aerosol Jet Printing of Strain Sensors for Soft Robotics," Advanced Engineering Materials, 26(1), p. 2301275, DOI: 10.1002/adem.202301275.

[15] Smith, B. N., Ballentine, P., Doherty, J. L., Wence, R., Hobbie, H. A., Williams, N. X., and Franklin, A. D., 2024, "Aerosol Jet Printing Conductive 3D Microstructures from Graphene Without Post-Processing," Small, 20(12), p. 2305170, DOI: 10.1002/smll.202305170.

[16] Meredith, A., Beuting, M., Trujillo, M., Sanders, S., and Andrews, J., 2024, "In-flight Imaging of Aerosol Jet Printer Droplets to Enable Spatially Resolved Flow Rate Measurements," Flexible and Printed Electronics, 9(1), p. 015003, DOI: 10.1088/2058-8585/ad1dbf.

[17] Chen, G., Gu, Y., Tsang, H., Hines, D. R., and Das, S., 2018, "The Effect of Droplet Sizes on Overspray in Aerosol-Jet Printing," Advanced Engineering Materials, 20(8), p. 1701084, DOI: 10.1002/adem.201701084.

[18] Ramesh, S., Mahajan, C., Gerdes, S., Gaikwad, A., Rao, P., Cormier, D. R., and Rivero, I. V., 2022, "Numerical and Experimental Investigation of Aerosol Jet Printing," Additive Manufacturing, 59, p. 103090, DOI: 10.1016/j.addma.2022.103090.

[19] Santaniello, T., and Milani, P., 2020, "Additive Nano-Manufacturing of 3D Printed Electronics Using Supersonic Cluster Beam Deposition," Frontiers of nanoscience, Elsevier, pp. 313-333, DOI: 10.1016/B978-0-08-102515-4.00012-X.

[20] Mosa, M. A., Jo, J. Y., and Kwon, K.-S., 2023, "Fast On-Off Jet Control of Aerosol Jet Printing (AJP) Using Internal Rotary Valve," Additive Manufacturing, 67, p. 103466, DOI: 10.1016/j.addma.2023.103466.

[21] Kim, M., and Lee, K., 2000, "Design Modification of Virtual Impactor for Enhancing Particle Concentration Performance," Aerosol Science & Technology, 32(3), pp. 233-242, DOI: 10.1080/027868200303768.